Monthly Notices of the ROYAL ASTRONOMICAL SOCIETY

MNRAS **506,** 6144–6158 (2021) https://doi.org/10.1093/mnras/stab1196
Advance Access publication 2021 April 28

Further support for a trio of mass-to-light deviations in Abell 370: free-form GRALE lens inversion using BUFFALO strong lensing data

Agniva Ghosh [1★] Liliya L. R. Williams [1★] Jori Liesenborgs [2] Ana Acebron,[3] Mathilde Jauzac,[4,5,6,7] Anton M. Koekemoer,[8] Guillaume Mahler,[4,5] Anna Niemiec,[4,5] Charles Steinhardt,[9,10] Andreas L. Faisst,[11] David Lagattuta[4,5] and Priyamvada Natarajan[12,13]

[1]*School of Physics & Astronomy, University of Minnesota, 116 Church Street SE, Minneapolis, MN 55455, USA*
[2]*UHasselt – tUL, Expertisecentrum voor Digitale Media, Wetenschapspark 2, B-3590 Diepenbeek, Belgium*
[3]*Dipartimento di Fisica, Università degli Studi di Milano, via Celoria 16, I-20133 Milano, Italy*
[4]*Centre for Extragalactic Astronomy, Durham University, South Road, Durham DH1 3LE, UK*
[5]*Institute for Computational Cosmology, Durham University, South Road, Durham DH1 3LE, UK*
[6]*Astrophysics Research Centre, University of KwaZulu-Natal, Westville Campus, Durban 4041, South Africa*
[7]*School of Mathematics, Statistics & Computer Science, University of KwaZulu-Natal, Westville Campus, Durban 4041, South Africa*
[8]*Space Telescope Science Institute, 3700 San Martin Drive, Baltimore, MD 21218, USA*
[9]*Cosmic Dawn Center, Denmark*
[10]*Niels Bohr Institute, University of Copenhagen, Lyngbyvej 2, DK-2100 Copenhagen Ø, Denmark*
[11]*Caltech/IPAC, MS 314-6, 1200 E. California Blvd. Pasadena, CA 91125, USA*
[12]*Department of Astronomy, Yale University, 52 Hillhouse Avenue, New Haven, CT 06511, USA*
[13]*Department of Physics, Yale University, P.O. Box 208121, New Haven, CT 06520, USA*

Accepted 2021 April 23. Received 2021 April 22; in original form 2020 December 29

ABSTRACT

We use the Beyond Ultra-deep Frontier Fields and Legacy Observations (BUFFALO) strong lensing image catalogue of the merging galaxy cluster Abell 370 to obtain a mass model using free-form lens inversion algorithm GRALE. The improvement of the strong lensing data quality results in a lens plane rms of only 0.45 arcsec, about a factor of two lower than that of our existing HFF v4 reconstruction. We attribute the improvement to spectroscopic data and use of the full reprocessed HST mosaics. In our reconstructed mass model, we found indications of three distinct mass features in Abell 370: (i) a ∼35 kpc offset between the northern BCG and the nearest mass peak, (ii) a ∼100 kpc mass concentration of roughly critical density ∼250 kpc east of the main cluster, and (iii) a probable filament-like structure passing N-S through the cluster. While (i) is present in some form in most publicly available reconstructions spanning the range of modelling techniques: parametric, hybrid, and free-form, (ii) and (iii) are recovered by only about half of the reconstructions. We tested our hypothesis on the presence of the filament-like structure by creating a synthetic cluster – Irtysh IIIc – mocking the situation of a cluster with external mass. We also computed the source plane magnification distributions. Using them, we estimated the probabilities of magnifications in the source plane, and scrutinized their redshift dependence. Finally, we explored the lensing effects of Abell 370 on the luminosity functions of sources at $z_s = 9.0$, finding it consistent with published results.

Key words: gravitational lensing: strong – galaxies: clusters: individual: Abell 370.

1 INTRODUCTION

For well over a decade lens modelling of clusters of galaxies has been an extraordinarily useful tool for revealing intrinsic properties of lensed sources at high redshifts. Clusters of galaxies can magnify faint distant background sources by increasing their angular extent and observed fluxes, and thus pushing them above the detection threshold of contemporary telescopes (Schneider, Ehlers & Falco 1992; Bartelmann 2010). By calculating the volume number densities of these sources one can estimate the ultraviolet luminosity function (LF), which helps in the understanding of the early galaxy evolution, their star formation rate, and thus their role in the reionization of the Universe (Bouwens et al. 2017b; Livermore, Finkelstein & Lotz 2017; Atek et al. 2018; Ishigaki et al. 2018).

To utilize clusters of galaxies as natural telescopes one needs to characterize their uneven optics, i.e. obtain magnification maps, which are directly related to the mass distributions in the clusters (Kneib & Natarajan 2011). This characterization is achieved by strong lens reconstruction algorithms, which use multiple images of background sources. Projected mass models of clusters obtained by strong lensing inversion techniques give the most detailed maps of cluster dark matter distribution obtained by any method.

With the contemporary observational techniques, the strongest cluster lenses have of the order of ∼100 multiple images spread across ≲1 arcmin. This number of constraints is inadequate to

★ E-mail: ghosh116@umn.edu (AG); llrw@umn.edu (LLRW)

break all lensing degeneracies, and thus the reconstructed mass distributions are usually not unique (Limousin et al. 2016; Priewe et al. 2017). However, since the inception of the Hubble Frontier Fields survey (HFF; PI: J. Lotz) using the *Hubble Space Telescope* (*HST*), a range of different lens inversion methods – which use different modelling assumptions and procedures – have made it possible to estimate systematic uncertainties based on different reconstructions of the same clusters of galaxies (Lotz et al. 2017). Comprehensive comparison projects were carried out based on synthetic clusters (Meneghetti et al. 2017), as well as observed HFF clusters (Priewe et al. 2017; Remolina González, Sharon & Mahler 2018), exploring systematic uncertainties in mass reconstructions (Raney et al. 2020b), probability of magnifications (Vega-Ferrero, Diego & Bernstein 2019), and recovered LF parameters of high-z galaxies (Bouwens et al. 2017a; Livermore et al. 2017; Ishigaki et al. 2018).

More recently, the Beyond Ultra-deep Frontier Fields and Legacy Observations (BUFFALO; PI: C. Steinhardt) program has embellished the HFF galaxy clusters by extending fields that are already covered by multiwavelength data from the *Spitzer Space Telescope*, the *Chandra*, and the *XMM–Newton* X-ray observatories and other ground-based observatories (Steinhardt et al. 2020). It has observed four times more than the existing HFF sky area for all six HFF clusters in five *HST* filters. Additional spectroscopic data from MUSE (Lagattuta et al. 2017, 2019; Richard et al. 2021) has also significantly contributed towards better lens reconstructions.

Reconstruction models can be broadly classified into two categories: parametric and free-form. Parametric models, which are more widely used, assign simple mass profiles – for example, Navarro–Frenk–White (NFW; Navarro, Frenk & White 1996) profiles, Pseudo Isothermal Elliptical Mass Distributions (PIEMD; Kassiola & Kovner 1993), pseudo-Jaffe distributions (PJ; Keeton 2001) – to observed galaxies, in association with luminosity–mass scaling relations, like the relation of Faber & Jackson (1976). In other words, the mass substructure in parametric models is always closely tethered to the observed luminosity distribution in clusters. The cluster-scale dark matter distribution is represented by the same or similar simple profiles, but with larger scale lengths, or by smoothed out galaxy light distributions (Natarajan & Kneib 1997; Zitrin et al. 2009).

In contrast to parametric models, free-form models (such as our method GRALE, see Section 2) do not assume any relation between the distribution of mass and light on the sky. In fact, GRALE does not have enough spatial resolution to account for the most compact baryonic distributions of many cluster galaxies (see Liesenborgs et al. 2020). The advantage of free-form methods is that they use the lensed images only, making them very sensitive to the information content of the lensed images. Parametric methods include strong priors in addition to images, so reconstructions are a compromise between image constraints and priors. While these priors are well motivated by astrophysics, they describe the average properties of galaxies and clusters, not specific properties that may differ between clusters and between individual galaxies, or deviate from averages, especially in merging clusters. Because of their unmitigated sensitivity to lensed images, free-form methods can detect cluster mass features that elude parametric methods. This is possible even with smaller numbers of images than in HFF, or with less than perfect data (see Section 3).

Abell 370 (hereafter A370), the subject of this paper, is the first massive clusters observed to be hosting gravitationally lensed images of background sources, namely the giant luminous arc in the southern part of the cluster. The cluster was studied in-depth and modelled by various groups starting in the mid-1980s (Hammer 1987; Soucail 1987; Soucail et al. 1988; Hammer & Rigaut 1989; Kovner 1989; Lynds & Petrosian 1989; Kneib et al. 1993). The first non-parametric reconstruction was done by Abdelsalam, Saha & Williams (1998). One of the first strong lensing models using the multicolour images from the refurbished *HST* Advanced Camera for Surveys (ACS) was created by Richard et al. (2010), and weak lensing analyses followed (e.g. Medezinski et al. 2011; Umetsu et al. 2011). Since the inclusion of A370 as one of the six HFF clusters in 2013, deeper imaging data became available. Eight different modelling groups produced mass distributions of the central cluster region, which are publicly available from the Mikulski Archive for Space Telescopes (MAST) website.[1]

Several parametric codes were used for A370 modelling in the HFF project. LENSTOOL was used by the Clusters As TelescopeS (CATS; Richard et al. 2014), the Johnson-Sharon groups (Johnson et al. 2014), and the works of Lagattuta et al. (2017, 2019). It utilizes a Bayesian Markov chain Monte Carlo sampler to optimize the modelling parameters. The overall mass distribution is modelled as a superposition of smooth large-scale potentials such as PIEMD and small-scale substructures that are associated with the locations of cluster member galaxies (Natarajan & Kneib 1997). Kawamata et al. (2018) used GLAFIC, a parametric method that models the halo components by an NFW profile and cluster member galaxies by a PJ profile. The Keeton group used the parametric LENSMODEL code, which in addition to large-scale haloes for the dark matter and/or hot gas, and small-scale haloes for cluster members, also includes small-scale haloes to model line-of-sight (LoS) galaxies (Raney, Keeton & Brennan 2020a). Among other parametric methods which submitted A370 models using HFF data but do not have a specific publication with their models, are Light Traces Mass (LTM; Zitrin & Broadhurst 2016), and PIEMDeNFW (Zitrin et al. 2013), used by the Zitrin group. LTM assumes that the dark matter distribution in the cluster can be approximately represented by the smoothed out luminous distribution. PIEMDeNFW uses PIEMD profiles for the cluster members, and elliptical NFW or PIEMD profile for the dark matter distributions.

Among the non-parametric modellers, Bradac-Hoag group used the free-form code SWUNITED (Strait et al. 2018) – the only A370 model which combines strong and weak lensing data. It uses an iterative χ^2 minimization process to solve for the gravitational potential on a grid. Our group worked with GRALE to model A370 with pre-HFF (Mohammed et al. 2016) and HFF data.

In addition to the above reconstructions, the Diego group used the hybrid method WSLAP+ (Diego et al. 2018; Vega-Ferrero et al. 2019), which decomposes the mass distribution into a free-form grid component for the diffuse mass, and a parametric component for compact member galaxies.

The main motivation behind this work is to present a comprehensive analysis of the cluster A370 using our free-form lens inversion method GRALE and utilizing the new strong lensing data from the BUFFALO collaboration, for the first time. The structure of this paper is as follows: Section 2 describes our free-form reconstruction method, GRALE, and the input images from the A370 BUFFALO catalogue. We discuss the reconstructed mass distribution in Section 3. In that section, we concentrate on how well mass follows light in the very core of the cluster (3.1), and on two possible mass features: a ∼100 kpc mass clump of roughly critical density in the eastern part of the cluster (3.2), and a filament-like structure passing North-South (N-S) through the cluster (3.3). In Section 4, we map the reconstructed magnification distributions in the source plane. Using

[1] https://archive.stsci.edu/pub/hlsp/frontier/abell370/models/

these, we estimate the probabilities of magnification in the source plane (4.3), and explore the redshift dependence of these probabilities as an indication of mass substructure (4.4). Finally, in Section 5, we estimated the lensed LF and its uncertainties, by convolving the reconstructed magnification distribution with the classical Schechter LF with the best-fitting parameter values taken from the literature.

Throughout this paper, we use the ΛCDM model of cosmology: flat, with matter density, $\Omega_m = 0.3$, cosmological constant density, $\Omega_\Lambda = 0.7$, and the dimensionless Hubble constant $h = 0.7$. The redshift of A370 is 0.375. The centre of the reconstruction region is at R.A. = 39.970°, Dec. = −1.577°. At the redshift of the cluster, 1 arcsec corresponds to 5.15 kpc.

2 RECONSTRUCTION METHOD: GRALE

2.1 Method

The lens inversion method used in this paper is based on the reconstruction code GRALE.[2] The publicly available GRALE software implements a flexible, free-form, adaptive grid lens inversion method, based on a genetic algorithm (Liesenborgs, De Rijcke & Dejonghe 2006; Liesenborgs et al. 2007; Mohammed et al. 2014; Meneghetti et al. 2017). It is ideally suited for reconstructions with numerous multiple images, available with *HST* data. The fact that the number of its model parameters exceeds the number of data constraints allows a fuller exploration of degenerate mass distributions (Mohammed et al. 2014; Sebesta et al. 2016, 2019; Williams, Sebesta & Liesenborgs 2018; Williams & Liesenborgs 2019). We refer the readers to see section 3.1 of Ghosh, Williams & Liesenborgs (2020, hereafter G20), for a concise description of the modus operandi of GRALE. In this work we used single lens plane inversion with GRALE. The current stable version of GRALE is not capable of doing multi-lens plane reconstructions.

2.2 Input

We are using the image data from the *HST* BUFFALO strong lensing multiple image catalogue. The catalog is made from fully reprocessed *HST* mosaics combining the HFF and BUFFALO data, as well as improved spectroscopic data. For A370, the catalogue consists of 170 strongly lensed images, in total. Spectroscopic data from the Multi-Unit Spectroscopic Explorer Guaranteed Time Observations (MUSE GTO; Lagattuta et al. 2017, 2019) confirmed spectroscopically 37 systems generating a total of 122 images. The images are visually flagged according to their qualities as GOLD, SILVER, BRONZE, or PLATINUM, by six different lens modelling groups associated with the BUFFALO collaboration. The GOLD images are those unanimously flagged as the good images. These are the most secure systems, with optical detection and spectroscopic confirmation. Out of the 37 spectroscopically confirmed systems, 31 are classified as GOLD systems. The other 6 spectroscopically confirmed systems from MUSE do not have secure identifications on the *HST* mosaics, with some being only tentatively detected or with multiple possible counterparts. These are classified as PLATINUM image systems. SILVER images are good quality images but are a bit less secure than GOLD, as they do not have spectroscopic confirmation but were still unanimously voted as multiple images. BRONZE systems are the worst quality images in the catalogue. These were not unanimously voted as multiple images and do not have spectroscopic redshifts. In this paper, we are using the most secured systems, 31 GOLD systems with spectroscopic redshifts and 8 SILVER systems with photometric redshifts, which are providing a total of 114 strongly lensed images. The images used in this work are listed in Table 1.

[2]https://research.edm.uhasselt.be/jori/grale2/

Table 1. Summary of the strong lensing images used from the BUFFALO catalogue of A370. Full table is available as online supplementary material. [L17: Lagattuta et al. (2017), K18: Kawamata et al. (2018), L19: Lagattuta et al. (2019)].

ID	R.A. (deg)	Dec. (deg)	z_{used}	Reference	Quality
1.1	39.967047	− 1.5769172	0.8041	L17, L19	GOLD
1.2	39.976273	− 1.5760558	0.8041	L17, L19	GOLD
1.3	39.968691	− 1.5766113	0.8041	L17, L19	GOLD
2.1	39.973825	− 1.584229	0.7251	L17, L19	GOLD
2.2	39.971003	− 1.5850422	0.7251	L17, L19	GOLD
2.3	39.968722	− 1.5845058	0.7251	L17, L19	GOLD
2.4	39.969394	− 1.5847328	0.7251	L17, L19	GOLD
2.5	39.96963	− 1.5848508	0.7251	L17, L19	GOLD
3.1	39.965658	− 1.566856	1.9553	L17, L19	GOLD
3.2	39.968526	− 1.5657906	1.9553	L17, L19	GOLD
3.3	39.978925	− 1.5674624	1.9553	L17, L19	GOLD
...					

We list here the differences between the image set used for the HFFv4 GRALE reconstructions and the one used in this work updated thanks to the BUFFALO data:[3]

(i) 4 new silver systems – 44, 45, 46, and 56.

(ii) 9 systems with new redshifts assigned to them – among them the systems 13, 14, 22, 25, 38, and 42 which are identified as GOLD systems with spectroscopic redshifts and systems 8, 11, 41, and 43 are SILVER systems with photometric redshifts.

(iii) 4 systems previously treated as GOLD and now classified as PLATINUM due to a lack of *HST* optical counterpart but with spectroscopic information from MUSE. These systems are 32, 33, 34, and 36. These systems are not used in this work.

(iv) System 16 has been newly flagged as BRONZE, and not used in this work. Image 16.2 is predicted but is not seen in either MUSE or *HST* data.

(v) Systems 10, 25, and 29 – third images are now flagged as BRONZE and are not used in this work.

The input to GRALE consists of the point image locations and redshifts only. In addition to the images, we also used a 250 × 250 arcsec null space region (see section 3.1 of G20), to discourage GRALE from generating fictitious images in regions of the lens plane where none are observed.

3 RECONSTRUCTED MASS DISTRIBUTION

Our best-fitting reconstruction is obtained by averaging 40 different and independent GRALE runs. Each starts with a random seed. While constrained by the required computational resources, this number is consistent with our previous works (G20; Sebesta et al.

[3]The changes in quality flags are made by a round of voting process by different mass modelling groups within the BUFFALO collaboration. The voting was mainly based on the quality and security of images and their associated spectroscopic information.

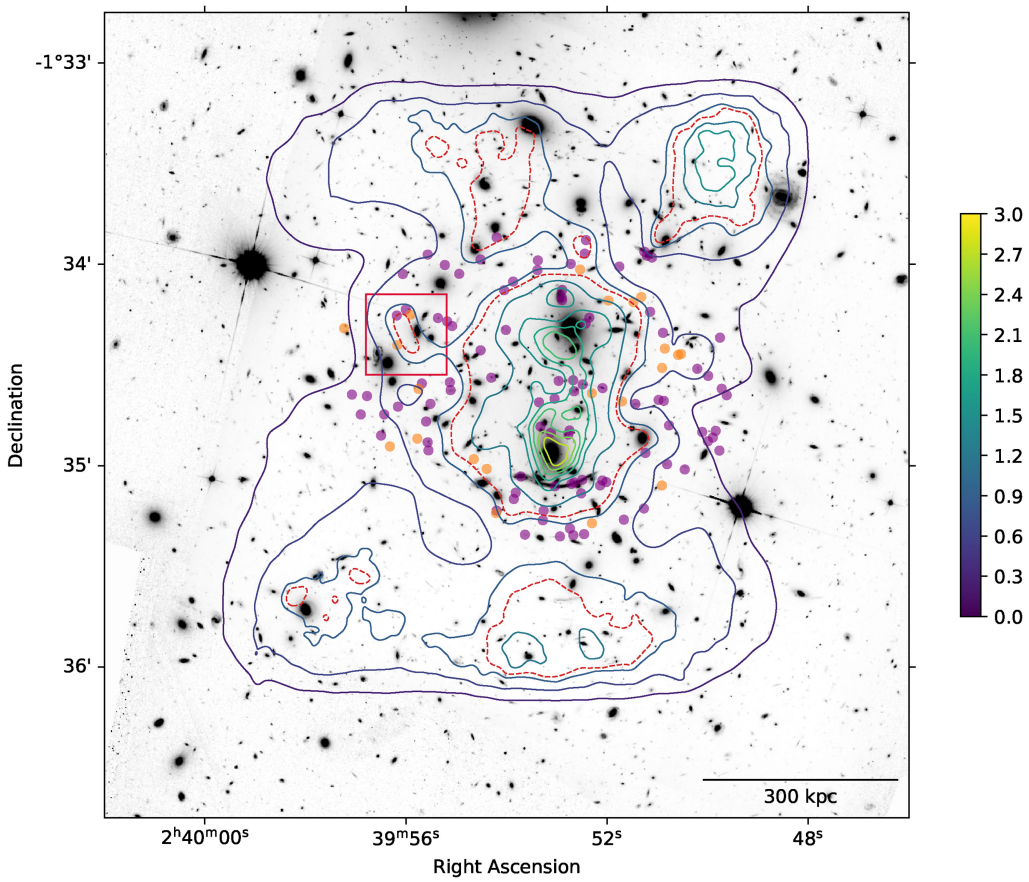

Figure 1. The coloured contours of GRALE reconstructed surface mass density distribution of A370 ($z_l = 0.375$) overlaid on the BUFFALO mosaic of A370 in the ACS/F814w filter. The surface mass density values are scaled by $\Sigma_{\rm crit,0}$. At $z_l = 0.375$, 1 arcsec corresponds to approximately 5.15 kpc. Red dashed contour corresponds to $\kappa = 1$. Filled purple dots mark the input images with spectroscopic redshifts (GOLD) and filled orange dots mark the input images with photometric redshifts (SILVER). The region in the red rectangle shows the approximate location of a substructure feature discussed in Section 3.2. The mass distributions ∼40 arcsec North and South of the cluster centre are discussed in Section 3.3.

2019; Williams & Liesenborgs 2019). In this work, we are using a reconstruction area of 0.927 Mpc by 0.927 Mpc and the smallest resolution cell (projected Plummer sphere) is about 12.5 kpc. The reconstructed mass distribution, overlaid on a BUFFALO image of A370 using ACS/F814w filter, is shown in Fig. 1. Contours represent the reconstructed projected surface mass density Σ, scaled by $\Sigma_{\rm crit,0} = c^2/4\pi G D_{\rm ol} = 0.314\ {\rm g\ cm^{-2}}$. The same reconstructed surface mass density plot is provided in the left-hand panel of Fig. 2. The right-hand panel of Fig. 2 shows the corresponding magnification distribution in the lens plane.

It is common to use lens plane rms (LPrms) as an indicator of how well a given mass model reproduces a cluster lens. The LPrms value for this reconstruction is 0.45 arcsec. This is an improvement over the earlier reconstruction of the same cluster using HFFv4 data which had LPrms of 0.88 arcsec. Since the total number of images used is nearly exactly the same in both cases, the reduced LPrms can be attributed to the improvement of the BUFFALO input data over the earlier HFF data.

Recent reconstructions by most methods in the literature produce low LPrms values, in the range ∼0.5 arcsec–1 arcsec. Yet the corresponding mass distributions, though sharing many similarities, tend to differ in the details. This is true not just for parametric versus free-form reconstructions, but among parametric models, even those sharing the same modelling software (Priewe et al. 2017).

In this section, we concentrate on three mass features that appear in our resulting mass map: the offset between the northern bright central galaxy (BCG) and the nearest mass peak, the ∼100 kpc mass concentration of supercritical density ∼250 kpc east of the main cluster, and a filament-like structure passing N-S through the cluster. Our reconstructions assume that all the deflecting mass is in the plane of the main lensing cluster. However, it is possible that some of these are foreground or background structures. It is interesting to note that all three features were detected as early as GRALE's HFFv1 reconstructions (Mohammed et al. 2016), later confirmed by HFFv4, and by the present BUFFALO work. It is even more interesting that all three features also appear to some extent in the first free-form reconstruction of Abdelsalam et al. (1998), using a different inversion method, although the details of these mass features differ (see their fig. 3).

The properties discussed below are summarized in Table 2.

3.1 Mass distribution near the BCGs

There are two clear central mass peaks in the reconstruction. The BCGs, associated with these central clumps are visible in the background BUFFALO image in Fig. 1. As one can notice, the southern mass clump closely follows the southern BCG on the plane of the sky, but the northern mass clump is significantly displaced

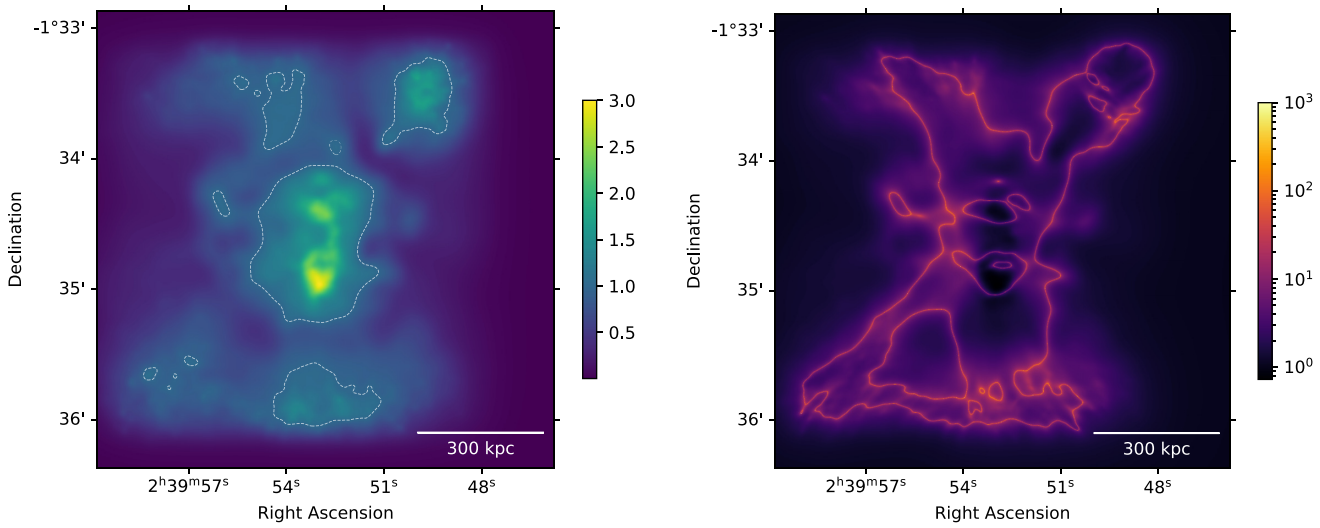

Figure 2. Left: GRALE reconstructed surface mass density distribution of A370, scaled by $\Sigma_{\rm crit,0}$. The dashed white contour represents $\kappa = 1$. *Right:* GRALE reconstructed magnification distribution of A370 in the lens plane ($z_{\rm l} = 0.375$) for sources at $z_{\rm s} = 9.0$.

Table 2. Summary of the different inversion methods' mass distribution of the three mass features identified in this paper. The works are classified as simply parametrized (SP), hybrid (HY), or free-form (FF), and are arranged approximately chronologically.

Model	Type	Mass peak near northern BCG	Mass feature Substructure 250 kpc east of centre	N-S filament (or similar external mass)
Abdelsalam et al. (1998)	FF	Displaced (∼30 kpc)	Present	Mass extension to the NW
LENSTOOL (Richard et al. 2010)	SP	Displaced (∼50 kpc)	Absent	None
LENSTOOL HFFv1 (Richard et al. 2014)	SP	Not Displaced	Absent	None
ZITRIN-LTM HFFv1	SP	Not Displaced	Absent	None
ZITRIN-NFW HFFv1	SP	Displaced (∼35 kpc)	Absent	None
GRALE HFFv1 (Mohammed et al. 2016)	FF	Displaced (∼20 kpc)	Present	Mass clumps near N and S boundaries
LENSTOOL (Johnson et al. 2014)	SP	Displaced (∼30 kpc)	Absent	None
LENSTOOL (Sharon HFFv4)	SP	Displaced (∼15 kpc)[a]	Absent	None
LENSTOOL (CATS HFFv4)	SP	Not Displaced	Additional DM halo	Two elongated, low density mass 'fingers'
GLAFIC (Kawamata et al. 2018)	SP	Displaced[b]	Absent	External shear present ($\gamma = 6.55 \times 10^{-2}$)
WSLAP+ (Diego et al. 2018)	HY	Displaced (∼40 kpc)	Present	None
GRALE HFFv4	FF	Displaced (∼15 kpc)	Present	Mass clumps near N and S boundaries
SWUNITED (Strait et al. 2018)	FF	Diffuse (∼15 kpc)	Absent	None
LENSTOOL (Lagattuta et al. 2019)	SP	Displaced (∼50 kpc)	Additional DM halo	External shear present ($\gamma = 1.28 \times 10^{-2}$)
LENSMODEL (Raney et al. 2020a)	SP	Not Displaced	Absent	None
GRALE BUFFALOv1 (this work)	FF	Displaced (∼35 kpc)	Present	Mass clumps near N and S boundaries

[a]The nearby halo is elongated NW-SE.
[b]There are two nearby haloes, one is ∼20 kpc away and the other one is ∼100 kpc away.

from the northern BCG (see Fig. 3). This possible example of mass not following light is consistent with the fact that A370 is an ongoing merger.

The offset we see between the northern BCG and the nearest massive mass clump is broadly consistent with the previous reconstructions performed by a number of groups using the HFF data (Richard et al. 2014; Kawamata et al. 2018; Strait et al. 2018). In our reconstruction, the displacement is ∼35 kpc South East (SE) of the northern BCG, comparable to that of the Lagattuta et al. (2019) model, where the centre of their DM3 halo is displaced by ∼50 kpc somewhat east of SE from that BCG. However, in another parametric model, Kawamata et al. (2018), there are two cluster-scale haloes near the northern BCG, one ∼20 kpc to the south, and the other located ∼100 kpc SE away from the northern BCG. Even though all models agree that there is significant mass not directly associated with the BCG to the SE of it, not all agree on the location, to within ∼50 kpc.

Since all models reproduce the image distribution very well, it is the lensing degeneracies (as well as the differences in input data) that lead to these disagreements. In this particular case, the main degeneracy is most likely the monopole (Saha 2000; Liesenborgs & De Rijcke 2012), because the ∼120 kpc region just SE of the northern BCG is devoid of lensed images, allowing any number of monopole-like redistribution of mass.

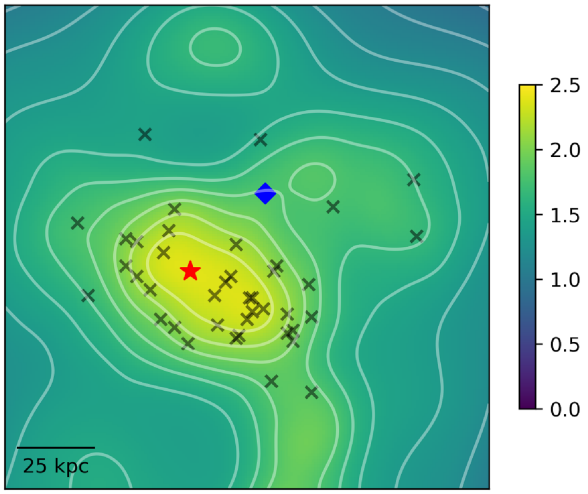

Figure 3. Region of the reconstructed mass distribution highlighting the offset between the northern BCG and the reconstructed northern mass clump. The red star shows the reconstructed northern mass peak from the average GRALE map. Position of the northern BCG is marked by the blue diamond. Nearby mass peaks from individual GRALE runs are shown as black crosses. The colour scale indicates values of κ in terms of $\Sigma_{\rm crit,0}$.

3.2 A $\sim 10^{12}$ $M_\odot$ substructure 250 kpc from cluster centre

A recent model comparison paper (Raney et al. 2020b) analysed half-sample mode of the magnification maps of the 6 HFF clusters. Half-sample mode is the maximum likelihood value of the magnification distribution at every pixel in the lens plane. They identified a mass feature in A370 that was independently recovered by a free-form GRALE, and a hybrid WSLAP+ method (see their fig. 17 and section 4.1.1). It is enclosed by the red rectangle in Fig. 1.

This feature is absent in most HFF parametric reconstructions, including the more recent ones (e.g. Sharon HFF v4; Kawamata et al. 2018; Raney et al. 2020b), as there is no light associated with it. Also, in Strait et al. (2018), which used the free-form code SWUNITED, the substructure is not seen. However, CATS HFF v4, Lagattuta et al. (2017, 2019) include it as an additional cluster-scale dark matter component, at a location very similar to where GRALE places it. This disagreement between recent reconstructions cannot be entirely due to the lack of lensing constraints: unlike the regions SE of the northern BCG, the $r \sim 50$ kpc ($\sim$10 arcsec) region centred on this mass clump has roughly five images. These variations in the mass reconstructions in this region are an example of lensing degeneracies, and not just between free-form or hybrid and parametric models, but among parametric models – CATS HFF v4 and Sharon HFF v4 – that use the same LENSTOOL software.

Our BUFFALO reconstruction also recovers this feature, giving more credence to its reality. It is the only feature with $\Sigma > \Sigma_{\rm crit,0}$ outside of the central cluster, and the mass clumps described in Section 3.3. The average surface mass density within that $\sim$100 kpc region is $0.9\Sigma_{\rm crit,0} (\approx 0.3\ {\rm g\,cm^{-2}})$, a factor of 1.3 larger than that in the surrounding regions. The total excess mass is 2.6×10^{12} $M_\odot$. Its relatively large mass is probably the reason why it was already detected more than 20 yr ago, by a different free-form lens inversion method (Abdelsalam et al. 1998). All the individual GRALE runs have produced this substructure. The distributions of mass within and around the substructure, as produced by individual GRALE runs, are presented in Fig. 4.

3.3 A North–South filament-like structure

Our reconstructed mass distribution (Fig. 1) contains significant mass clumps, located $\gtrsim$40 arcsec ($\gtrsim$200 kpc) above and below the central region, which do not represent actual mass at those locations. These fictitious mass clumps are generated by GRALE in order to minimize the fitness values for the given set of input images, i.e. to reproduce the observed image positions as best as possible. This can be attributed to GRALE trying to compensate for an otherwise unobserved mass outside the strong lensing region, which, as we illustrate below, is consistent with a filament-like structure passing through this cluster. These probably lie well outside the strong lensing region, and must be sufficiently massive to influence the deflection angles of the lens in the central part, and thus the strongly lensed image locations.

Though no other reconstruction of A370 has such fictitious masses, many include features that result in similar influence on the image locations. CATS HFF v4 reconstructed mass map includes two highly elongated, low density mass 'fingers' with an angle of $\sim$40 degrees between them, arranged in an X-like pattern, centred roughly on the cluster centre and extending N-S well beyond the strong lensing region (see their mass models on MAST[4]). We suspect that these have the same role as our external mass clumps.

In the GLAFIC reconstruction of Kawamata et al. (2018), the authors include an external shear of $\gamma = 6.55^{+2.25}_{-2.35} \times 10^{-2}$ with a position angle of $\theta_\gamma = 177.71^{+4.13}_{-5.64}$ degrees at a redshift $z = 2$ (see their table 8). External shear is often used to account for mass located outside the modelled region. Its orientation is consistent with our speculation of the presence of outlying mass structures, above and/or below the central region of the cluster.

Lagattuta et al. (2019) model also has external shear, $\gamma = 0.128$, whose inclusion considerably decreases the model's LPrms from about 1 arcsec to 0.66 arcsec. To replace the external shear with a more physically motivated component, the authors carry out a useful exercise of figuring out what mass distribution could be responsible for the shear. They test a few possibilities and conclude that the mass associated with the observed background, foreground, and in-cluster galaxy groups are not responsible for the shear. This leaves mass further afield as the only possibility, consistent with our conclusions.

It is interesting to recap how GRALE and the LENSTOOL-based parametric analysis of Lagattuta et al. (2019) localized the mass responsible for the external shear. GRALE, being sensitive to images only, must have picked up on the small systematic image deflections, tracing their source to outside (above and/or below) the cluster's central $\sim$400 kpc region. The parametric model, on the other hand, had to try a number of possible sources of mass and rule them out one by one if they did not produce a better fit. For a discussion on how deflection fields are affected by external mass clumps, see the work of Mahler et al. (2018) on the cluster Abell 2744.

Lagattuta et al. (2019) also pointed out the possibility of additional mass structures in the outskirts of A370 as a replacement to their external shear. In their fig. 11, they showed several concentrations of galaxies with similar colours to cluster members, in the lower resolution image taken on the Canada–France–Hawaii Telescope (CFHT) with CHF12K (Hoekstra 2007). The blue contours in that figure show smoothed out light distribution from the cluster red sequence members. One can see mass structures towards North North West and South of SE, and within the virial radius. Spectroscopic redshift measurements for a few of these objects by early CFHT/PUMA and

[4]https://archive.stsci.edu/prepds/frontier/abell370_models_display.html

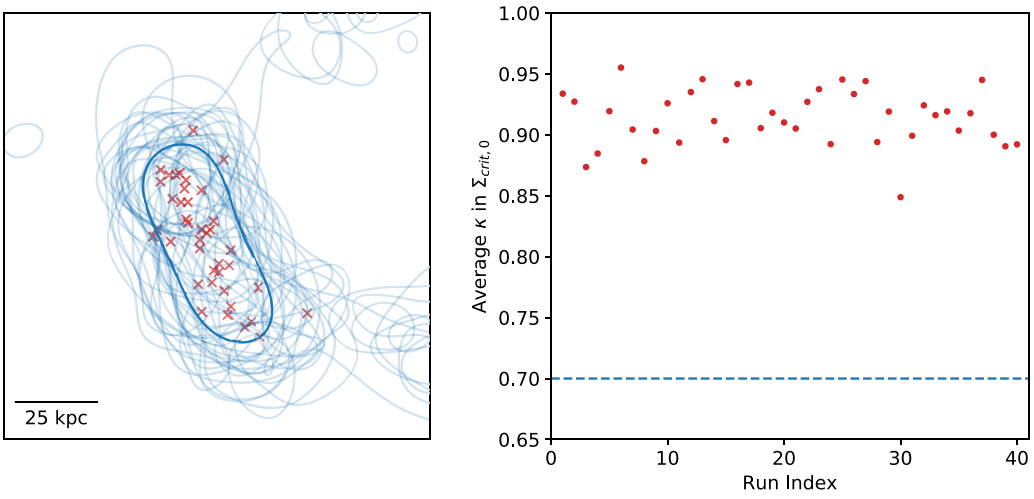

Figure 4. Left: Region of the reconstructed mass distribution highlighting the $\sim 10^{12}$ $M_{\odot}$ substructure 250 kpc from the cluster centre. Dark blue contour represents the $\kappa = 1$ of the average GRALE map, where κ is in terms of $\Sigma_{\rm crit,0}$. Light blue contours represent the $\kappa = 1$ contours produced by 40 individual GRALE runs. Red crosses mark the points with maximum convergence within the substructure, as produced by the individual GRALE runs. Right: Average κ values in terms of $\Sigma_{\rm crit,0}$ within $\sim$100 kpc region around the substructure for each individual GRALE runs. Dashed blue line shows the average background κ around the substructure.

ESO/PUMA2 (Fort et al. 1986) placed them at the same distance as the cluster (see fig. 1 in Mellier et al. 1988). The size and locations of these structures are promising as a source for the additional structures GRALE has produced.

In the following subsection, we present the GRALE analysis using a synthetic cluster, which reinforces the conclusion that A370 likely has a filament-like structure passing N-S through/near it.

Our conclusion from considering the three mass features described above is that many models agree on these (though not necessarily down to fine details) in the reconstruction of A370. The interesting point is that the models that agree with each other are not all of the same modelling type (for example, not all are parametric), but span the range of modelling philosophies: parametric, hybrid, and free-form. At the same time, some models of the same type, and even the same modelling software, disagree with each other.

3.4 Modelling a synthetic cluster with filament: Irtysh III

Our hypothesis for the origin of the fictitious mass clumps towards the top and bottom edges of the reconstructions (Section 3.3) is that these replicate the effect of actual mass structures lying well outside the reconstruction region. The presence of these masses minimizes the fitness value of the overall reconstruction, i.e. better reproduces the observed images. To verify this hypothesis, we performed a reconstruction of a synthetic cluster which mocks a situation with filament-like structures placed well outside of the cluster strong lensing region.

3.4.1 Method

In G20, we worked with the synthetic cluster Irtysh to show that the increasing number of input images improves the quality of the lens reconstruction, and has the potential to predict the Hubble's constant with $\lesssim$1 per cent precision. On the contrary, the LPrms value increases, counter-intuitively, due to the complexity of fitting the increasing number of constraints from strongly lensed images.

Since we had two other versions of Irtysh, Irtysh I, and II, thoroughly examined in G20, the version of Irtysh used in this paper is named Irtysh III.

For simplicity and computational efficiency, the mass distributions for these mock galaxy clusters were generated using the analytical softened power-law ellipsoid potential called `'alphapot'` from the GRAVLENS catalogue of models (Keeton 2001), to represent the cluster-scale and the galaxy-scale projected lensing potential,

$$\Psi = b(s^2 + \xi^2)^{\frac{\alpha}{2}}, \tag{1}$$

where b is the normalization, s is the core radius that eliminates the central singularity, and $\xi^2 = x^2 + y^2/q^2 + K^2xy$ with q and K together representing ellipticity with non-zero position angle. Because the cluster is synthetic, this mass distribution can be rescaled to any size.

The advantage of using an analytical potential is that the values of the deflection angles and the surface mass density can be determined exactly. We also note that the profiles we use to build up our synthetic clusters i.e. the elliptic potential `alphapot`, are different from the basis functions GRALE uses for reconstruction, which are projected Plummer spheres.

Irtysh III is made as a superposition of two massive cluster-scale dark matter components, and 115 galaxy-scale components. The number and normalizations of the latter are determined by assuming the mass function for clusters of galaxies (Press & Schechter 1974; Bahcall & Cen 1993). In order to mock a cluster with outlying masses, two identical large elliptical mass clumps, each 88.1 per cent of the central cluster mass, were placed at a distance of 180 arcsec (0.967 Mpc) from the cluster centre, above and below the central region. They remain significantly outside the strong lensing region that GRALE uses in reconstructions. The true projected mass distribution of Irtysh III is shown in the upper panel (left: 2D; right: raised relief map) of Fig. 5.

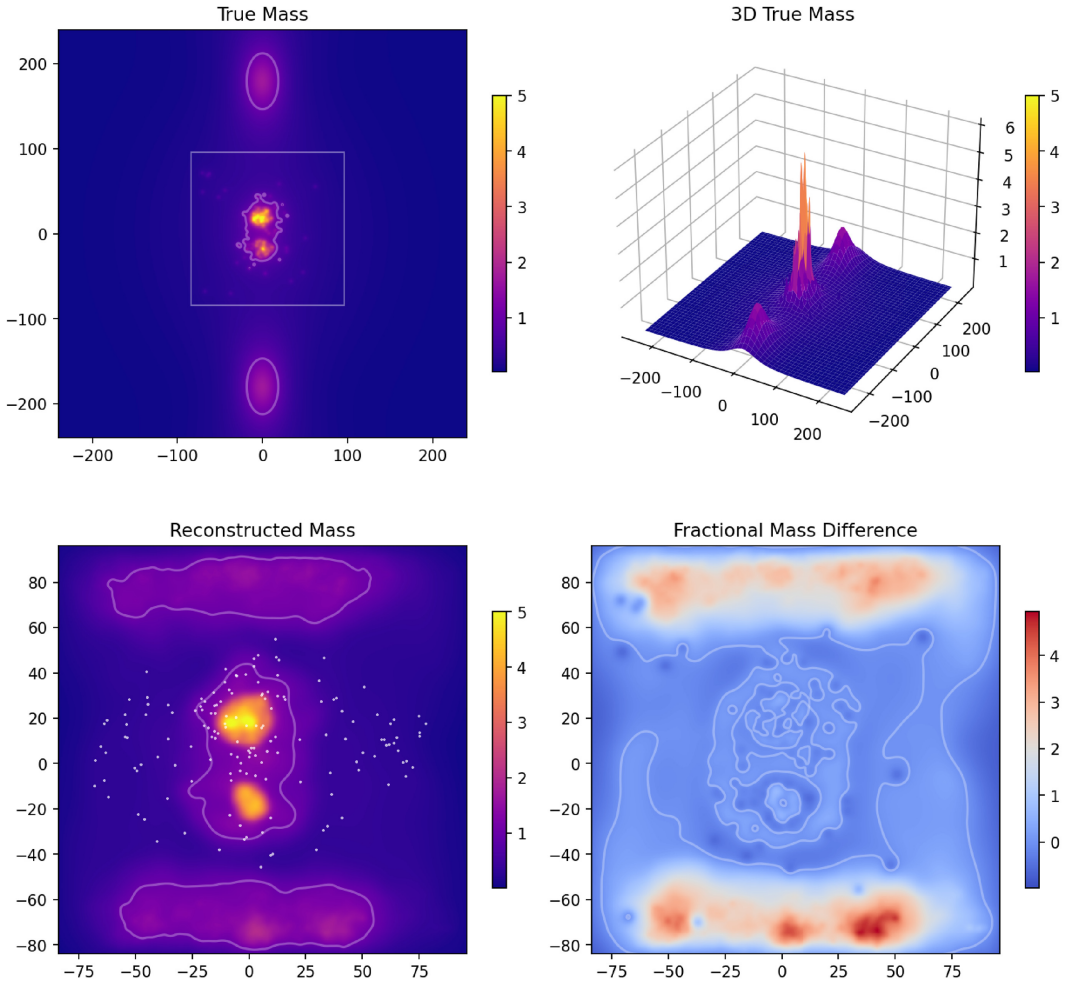

Figure 5. Mass distribution maps for the synthetic cluster Irtysh IIIc. Upper left: True surface mass density distribution. The white box represents the region used for reconstruction. There are two outer mass clumps lying well outside this box. Faded white lines represent the $\kappa = 1$ contour. Upper right: 3D presentation of the true surface mass density distribution. Lower left: Reconstructed surface mass density distribution. White points represent the input images used in GRALE, and the faded white lines represent the $\kappa = 1$ contour. Lower Right: The fractional mass difference ($\Delta m/m$, as defined in equation 2) map between the true and the reconstructed surface mass densities. Faded white contour represents the $\Delta m/m = 0$ contour. According to the colour scheme, overestimated mass is represented as more red and underestimated mass as more blue. In all of these maps, the surface mass density values are scaled by $\Sigma_{\rm crit,0}$.

3.4.2 *Input*

We assumed the cluster to be at a redshift of $z_{\rm l} = 0.4$. We are using 151 input images for the reconstruction of Irtysh III. This means this is the 'c' type of reconstructions following the notation used in G20. The 'a' and 'b' type of reconstructions are those with about 1000 and 500 input images, respectively. The images were produced following the procedure described in section 2.3 of G20.

3.4.3 *Results*

The reconstructed best-fitting mass distribution is obtained by averaging 40 different and independent GRALE runs. It is shown in the lower left panel of Fig. 5. The colour bar represents projected surface mass density Σ, scaled by $\Sigma_{\rm crit,0} = c^2/4\pi GD_{\rm l} = 0.314\ {\rm g\,cm^{-2}}$. As per our expectations, GRALE has produced fictitious mass clumps above and below the cluster centre, in regions with no observed images. GRALE created these clumps to replicate the effect of true mass structures lying outside the reconstructed region, in order to minimize the fitness of the reconstruction. The LPrms of this reconstruction is 0.21 arcsec.

If the fictitious outer mass clumps in the reconstructions are mimicking the deflection field produced by the filament-like mass clumps in the true Irtysh III, we expect the masses and distances of the two sets of clumps to scale according to the scaling relation of external shear.

In the true mass distribution, each of the upper and lower outer masses are about 88.1 per cent of the central cluster mass. They are at a distance of 180 arcsec from the cluster centre, whereas in the reconstruction the upper and lower mass clumps are at a distance of ∼80 arcsec. The external mass contribution to the deflection field in the central region varies as $\sim M/r$, where r is the distance of the external mass clumps from the cluster centre, and M is the external mass. Therefore, one would expect the amount of mass in the upper or lower clumps in the reconstruction to be approximately, 88.1 per cent $\times \frac{80\,\rm arcsec}{180\,\rm arcsec} \simeq 39$ per cent. The average reconstructed masses in the upper and lower clumps are about 63 per cent and 57 per cent of the reconstructed central cluster mass, respectively.

This is fairly comparable to our estimate above, indicating that GRALE is sensitive to mass outside of the image region, and replaces distant mass clumps with scaled masses inside the reconstruction box, but outside the image region.

In the lower right panel of Fig. 5, the fractional mass difference map is shown. This quantity is defined as

$$\frac{\Delta m}{m} = \frac{m_{\rm reconstructed} - m_{\rm true}}{m_{\rm true}}. \quad (2)$$

The value of this quantity determines whether GRALE has overestimated or underestimated the mass in a certain region. Clearly, near the fictitious mass clumps the fractional mass difference is quite high. On the contrary, it is small near the central mass peaks and the smaller mass peaks of the true mass distribution. For the very small true mass peaks, GRALE does not have enough constraints and/or enough angular resolution to resolve them separately.

The fictitious mass clumps in the reconstruction of Irtysh III look very similar to those in A370, which strengthens our hypothesis that A370 has a filament-like structure running N-S through it.

4 RECONSTRUCTED MAGNIFICATIONS

4.1 Magnification distribution in the source plane

To calculate the magnification distribution in the source plane of A370, we used the best-fitting reconstruction, which is an averaged combination of all the 40 individual GRALE runs. We generated an 120 × 120 arcsec grid in a source plane of a given redshift, with a grid spacing of 0.25 arcsec. Considering each of the grid points as a point source, we forward lensed them using the reconstructed deflection angles and the lens equation. In this way, we generated one or multiple images for each of the points in the source plane grid. Then, we calculated the sum of the unsigned magnifications for all the images in the image plane, generated from a single source point, and assigned it to be the magnification of that corresponding source. This produces the reconstructed magnification distribution in the source plane.

We want the readers to note that our method of calculating the magnification distribution in the source plane differs from the source plane and the image plane methods described in Diego (2019) and Vega-Ferrero et al. (2019). For a comparative discussion, see Appendix A.

The left-hand panel in Fig. 6 shows the best-fitting magnification distribution in a source plane at a redshift of $z_{\rm s} = 9.0$. One can easily notice the caustics i.e. the contours of high – theoretically infinite – magnifications.

Since we are using an average of 40 different GRALE runs, magnification maps can also be obtained for each of these GRALE runs individually, giving rise to the reconstructed range of the source plane magnification distributions. The right-hand panel of Fig. 6 plots a normalized superposition of the 40 individual A370 reconstructions. In this range of maps, one can see the caustic features from all the individual runs.

An interesting outcome of this exercise is shown in the right-hand panel of Fig. 6: in the normalized superposition of range magnifications maps the caustics from 40 individual runs are not completely overlapping with each other. Rather, they are shifted significantly either towards the top or the bottom of the source plane for different runs, creating an overall fuzzy appearance. The main reason for these shifts is that, for different individual runs, GRALE produces different amounts of extra mass in the clumps towards the northern and southern edges of the central region.

Earlier we noted the presence of these mass clumps in the best-fitting maps of A370, and argued that they are due to a filament-like structure outside of the modelling window. We now see that individual maps distribute the mass differently between northern and southern edges. It is interesting to compare this with the synthetic cluster Irtysh III, which was constructed with filament-like structures north and south of the lens centre.

In the left-hand panel of Fig. 7, we show the best-fitting magnification distributions in the source plane of Irtysh III. As in the case of A370, the reconstructed range distribution of the source magnification maps shows that the caustics are shifted up and down for individual GRALE runs (right-hand panel of Fig. 7). This similarity between the reconstructions of A370 and Irtysh III strengthens our hypothesis that the extra outlying mass clumps are due to filament-like structures above and/or below the main cluster. It is also worthwhile to mention that for the GRALE reconstructions of synthetic Irtysh Ic – where no external filament-like masses were present and no extra mass clumps were created by GRALE (see G20) – all the caustics in the range magnification maps are superimposed, unlike those in Irtysh IIIc and A370 (see Fig. 8).

4.2 Relation between outer mass clumps and back-projected images

In the previous subsection, we concluded that individual GRALE runs produce different amounts of extra mass towards the northern and southern edges of the central region, causing vertical shifts in the caustics. For a further verification of this argument, we calculated the vertical shifts, Δy, for each of the back-projected images in the source plane, and for each individual run, from their averaged back-projected positions in the best-fitting reconstruction. Caustics trace out the source plane positions with theoretically infinite magnifications. Therefore, the vertical shifts of back-projected images (which are basically the reconstructed source positions) are directly related to the shifts of the caustics. If our hypothesis holds, Δy should be related to the ratio of the amounts of mass lying outside ±50 arcsec from the cluster centre, in the northern and southern directions.

In the left-hand panel of Fig. 9, we plot the vertical shifts of the back projected images against these mass ratios for each of the 40 GRALE runs of our A370 reconstructions. The plot shows only the first source with three images. Each of these three back projected images are marked by three different colours, red, green, and blue. The annotated numbers by the sides of the plotted points mark the corresponding GRALE run number. As one can see, Δy is more positive when the northern edge has a greater amount of extra mass (the mass ratio is higher), and is more negative when the southern edge has more mass. The rest of the sources exhibit similar trends. These clearly imply that GRALE generates degenerate solutions for individual runs by varying the fraction of mass in the upper versus lower mass clumps.

Now, it is interesting to check whether the vertical shifts of the caustics and ratio of the upper to lower masses are also related in the same fashion for Irtysh III. This is shown in the right-hand panel of Fig. 9, for the case of the first source with three images. The trend of the points plotted is very similar to what we saw in A370. Other sources for Irtysh III also exhibit analogous trends. The similarity of these results for Irtysh III with A370 certainly implies that the shifting of the back projected images and caustics is proportional to the mass ratio of upper and lower extra mass clumps.

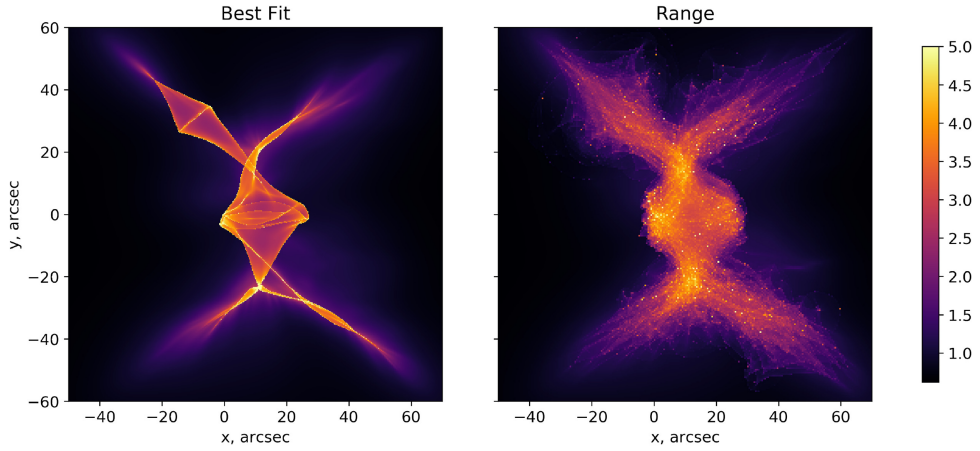

Figure 6. Magnification maps for A 370 in the source plane at a redshift of $z_s = 9.0$. The left-hand panel shows the best-fitting magnification maps i.e. magnification values are generated from the average of all the 40 GRALE runs. The right-hand panel shows the normalized superposition of the range distribution of magnifications in individual GRALE runs in the source plane. In other words, the left-hand panel shows the magnification of the average and the right-hand panel shows the average of magnifications.

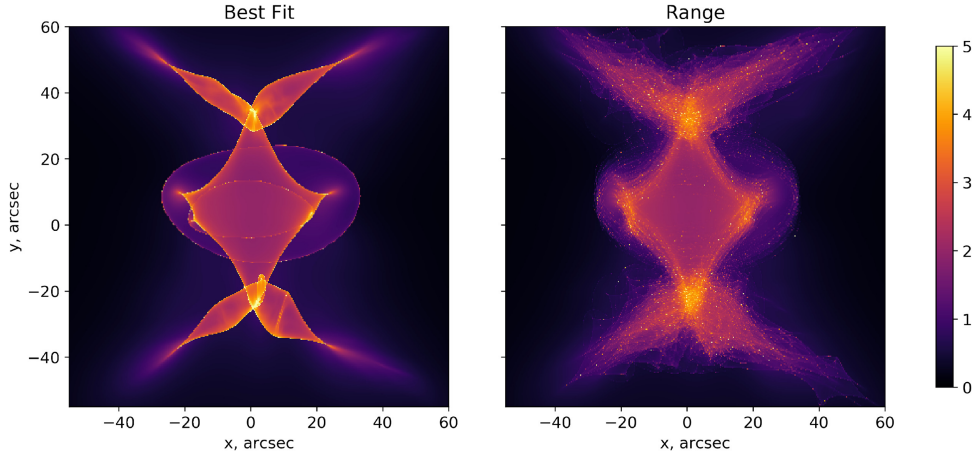

Figure 7. Same as Fig. 6 but for synthetic cluster Irtysh IIIc; see Fig. 5.

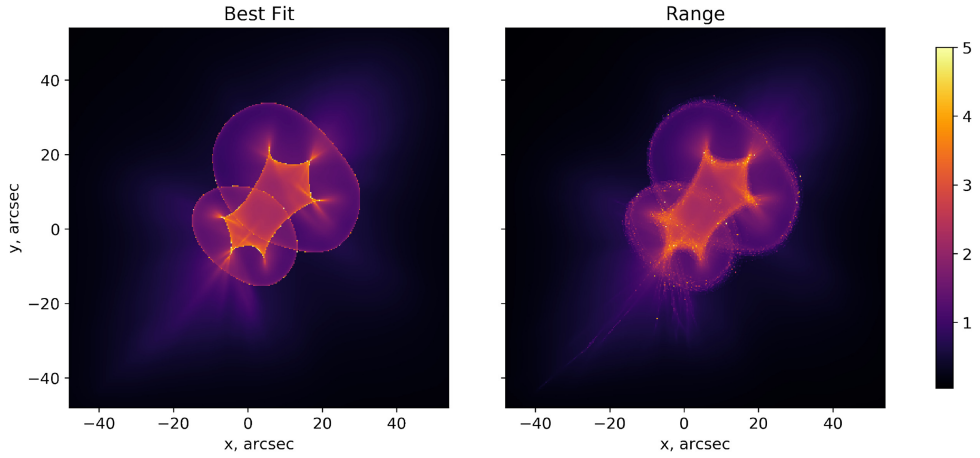

Figure 8. Same as Fig. 6 but for synthetic cluster Irtysh Ic (see G20).

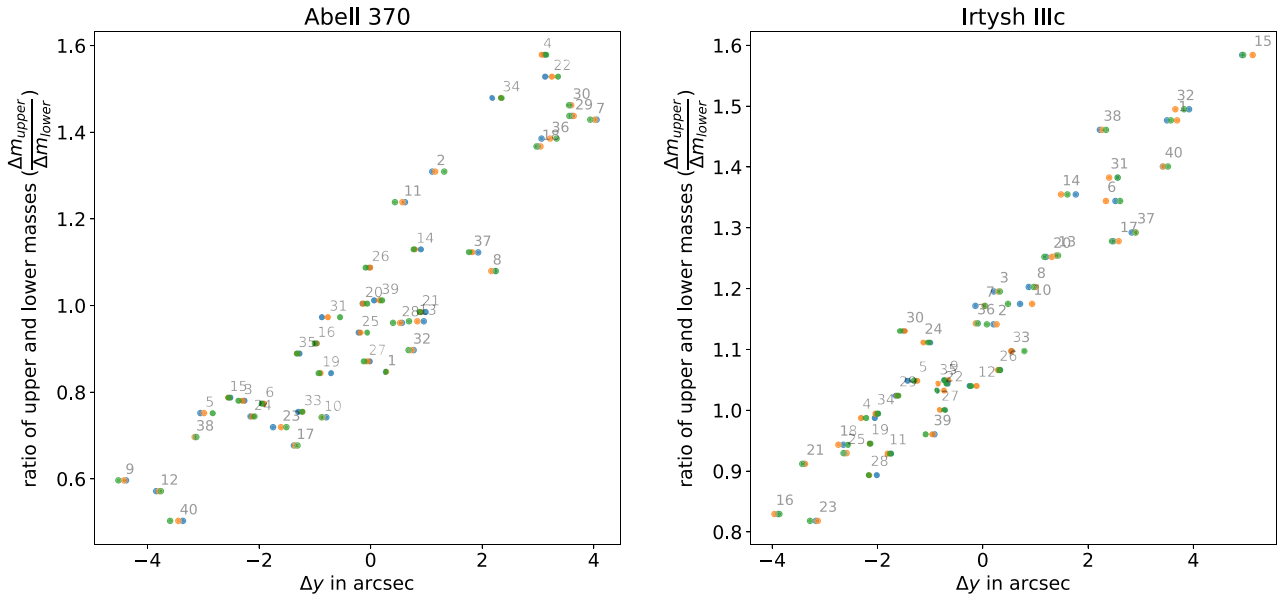

Figure 9. Ratio of the outer upper and lower masses as a function of the vertical shifts of the back projected images for individual GRALE runs for A370 (left) and Irtysh IIIc (right) reconstructions. We are considering only the first source in the catalogues for each of the clusters. In both cases, there are three multiple images each represented by different colours. The numbers annotated beside the set of points are representing the 40 GRALE runs.

Thus, we are reasonably confident in concluding that there exist outlying masses, well outside to the north and the south of the strong lensing region in A370. It is possibly a filament-like large scale structure passing through the cluster of galaxies. We expected to see this filament in weak lensing reconstructions, but Strait et al. (2018), who use both strong and weak lensing data, do not seem to have it in their mass maps. However, their field of view of ∼1 Mpc may be too small to detect a filament.

4.3 Probabilities of magnification in the source plane

Galaxy clusters are often used as nature's telescopes to magnify very high redshift sources (Bouwens et al. 2017b; Livermore et al. 2017; Atek et al. 2018; Ishigaki et al. 2018). The ultimate goal is to estimate the source LF, but an intermediate step, which we carry out in this subsection, is to obtain a statistical characterization of a cluster's magnifying power, i.e. a probability distribution of source plane magnifications.

The probability of magnification in the source plane can be defined as the fraction of the area in the source plane at a given redshift, z_s, that has an unsigned magnification value larger than a given value μ (Wong et al. 2012; Diego 2019). We denote this quantity by $\sigma_{sp}(\mu, z_s)$. Our definition of $\sigma_{sp}(\mu, z_s)$ differs from the more common definition of the quantity where physical source plane area is considered. $\sigma_{sp}(\mu, z_s)$ will be later used to estimate the number of galaxies expected to be observed above a given detection threshold, i.e. the lensed LF (see Section 5).

Near a caustic, this probability is proportional to the probability of a source point to be closer than a distance $\Delta\beta$ from the caustic. This relation can be approximated to $\sigma_{sp} \propto \sqrt{\Delta\beta^{-1}} \propto \mu^{-2}$, (see chapter 11 of Schneider et al. 1992). Thus, for high magnifications, σ_{sp} versus μ in the log–log space can be approximated by a straight line with a slope of −2.

Using the best-fitting GRALE reconstruction we computed the magnification maps in the source plane, as described in Section 4.1, at a redshift of $z_s = 9.0$. From these magnification maps, we estimated the probability of magnification, σ_{sp}, for the given source plane area. Fig. 10 shows σ_{sp} as a function of magnifications (μ), in log–log space, for different reconstructions of A370 (with HFFv4 and BUFFALO data) and Irtysh (I, II, and III; c reconstructions only, with 151 images). The best-fitting distributions are shown by solid coloured lines and the shaded coloured regions show the uncertainties

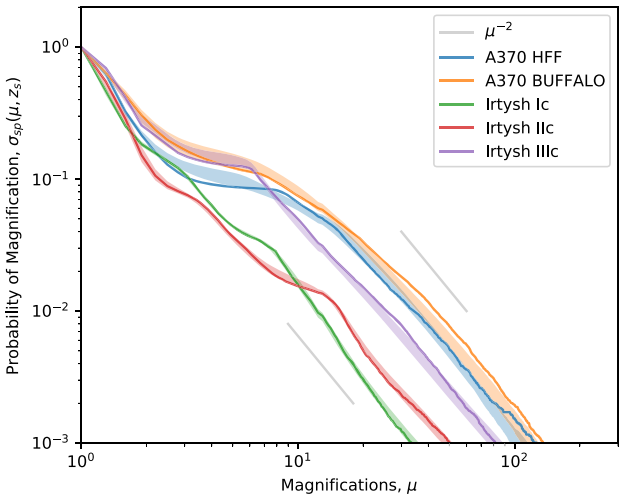

Figure 10. Cumulative probabilities of magnification, $\sigma_{sp}(\mu, z_s)$, as a function of magnifications (μ) for A370 HFF and BUFFALO reconstructions and Irtysh c reconstructions (with ∼150 images), for sources at $z_s = 9.0$. Coloured shaded regions are showing the uncertainties in the probabilities (68 per cent confidence range) for the corresponding cluster. Grey lines denote a slope of μ^{-2}. The μ^{-2} behaviour of the probabilities is evident for higher magnification values. The normalization of the curves is arbitrary for different clusters given that the source plane area we have considered are different for each of them.

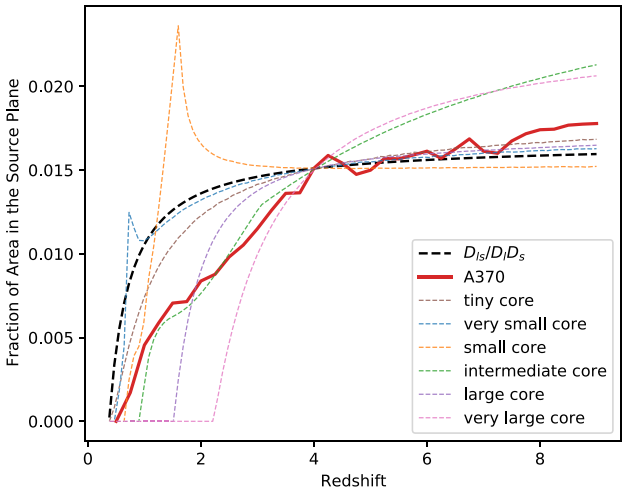

Figure 11. Redshift dependence of the probabilities of magnification in the source plane. Red line denotes the fractional area in the source plane with magnifications greater than 30, $\sigma_{sp}(\mu = 30, z_s)$ for A370. To reduce the computational time a coarse source plane grid was chosen for this exercise, which in turn produced a less smoother curve. Black dashed line shows the relation $\theta_E^2 \propto D_{ls}/(D_l D_s)$, normalized by $\sigma_{sp}(\mu = 30, z_s = 4)$ of A370. The coloured dotted lines show the source plane redshift dependence of $\sigma_{sp}(\mu = 30, z_s)$ for a six single circularly symmetric lens with varying core sizes, normalized by $\sigma_{sp}(\mu = 30, z_s = 4)$ of A370.

in the probabilities obtained from 40 different GRALE runs. The grey lines in the figure represent the slope of -2. It can be seen that, for magnifications above 10, the expected μ^{-2} behaviour is fairly maintained in all of the reconstructions.

At lower magnifications, the shape of the magnification probability distribution depends on the details of the mass distribution. In Fig. 10, we see flat plateaus in the probability curves between the magnification values 2 and 10 for both A370 and Irtysh IIIc, whereas for Irtysh I and II, the μ^{-2} behaviour is maintained even at lower magnifications. We speculate that these are due to the presence of naked cusps and diamond caustic folds that are outside the oval caustic in the source plane for A370 and Irtysh IIIc, which, in turn, are mostly due to the masses above and below the main cluster (see Figs 6 and 7). Near these regions, the magnification values tend to change very rapidly. In contrast, Irtysh I and II have no such naked cusps (see Fig. 8 for Irtysh I) and thus have less abrupt changes in slope values of the probabilities for low magnifications.

4.4 Redshift dependence of the magnification probabilities

Here, we continue to examine how the magnification properties of a cluster are related to those of its mass distribution. In the previous subsection, we used a fixed $z_s = 9.0$, and varied magnification μ. Here, we fix μ, and vary z_s.

For a given z_l, the area in the source plane, $\sigma_{sp}(\mu, z_s)$, where sources at a redshift z_s must lie in order to be magnified by greater than a certain unsigned value, μ, is a function of the source redshift and the amount and nature of substructure, or clumpiness in the lens. This was nicely highlighted by Vega-Ferrero et al. (2019). The naive dependence on z_s, which ignores clumpiness, scales as the solid angle subtended by a disc of critical density with the Einstein radius, and is given by $\theta_E^2 \propto D_{ls}/(D_l D_s)$. It is shown as the black dashed line in Fig. 11. (Note that the absolute normalization of the curve is not important.)

The actual dependence on z_s is more complicated because of the clumpiness in the lens; we will examine it here, in a simplified form. We consider a single circularly symmetric lens, i.e. a substructure, with a range of core radii (six dotted curves in Fig. 11). A realistic lens will have many such substructures.

There are two ways that a given mass distribution can attain high magnifications, say $\mu > 30$. The lens must either be supercritical, or sub-critical, with $1 - \mu^{-1/2} \lesssim \kappa < 1$.

A lens with a small enough core will be supercritical even at low z_s. An example is the orange dotted line in Fig. 11. There is a small flattening of the curve at $z_s \approx 0.8$, where the lens becomes supercritical. At higher z_s, it has two critical curves, radial, and tangential, so there are two annular regions in the lens plane with $\mu > 30$. As z_s increases, the lens plane region between them drops to lower magnifications. The source redshift where it just falls below $\mu = 30$ corresponds to the location of the spike in Fig. 11; for the orange curve that happens at $z_s \approx 1.5$. These two features – transition to supercritical and behaviour of the region between the two critical curves – are also visible in other dotted lines even though for some they are barely visible, like in the green curve at $z_s \approx 3.0$.

The set of six dotted curves – from the tiny to very large core – shows the full range of behaviour; all normalized to go through the same σ_{sp} at $z_s = 4.0$.

A cluster mass distribution can be approximately thought of as a superposition of many power-law lenses with varying normalizations, and core sizes. Equivalently, one can think of power spectrum of projected density fluctuations (Mohammed et al. 2016). If singular, or small-core substructures dominate, the overall σ_{sp} for a cluster lens will follow $\theta_E^2(z_s)$, especially at higher z_s. This is the case for most of the cluster models presented in Vega-Ferrero et al. (2019): their substructures (i.e. galaxies) tend to be sub-critical for $z_s \lesssim 2$, and supercritical for sources at higher redshifts.

Our reconstruction of A370 is represented by the thick solid red line in Fig. 11, and shows a somewhat different behaviour. It grows slower with z_s compared to models in Vega-Ferrero et al. (2019), and continues to grow, though at a slower rate even past $z_s \sim 4.0$. This is consistent with the visual impression of GRALE's reconstructions compared to that of many other methods: its substructure is more extended, or diffuse. Furthermore, the fact that its σ_{sp} continues to grow for all z_s means that the density fluctuation power spectrum has power on a much wider range of scales compared to that of other lens inversion methods. This conclusion is consistent with the analysis of Mohammed et al. (2016); see their fig. 9. We note that A370 has a much more complicated structure compared to the simplified analysis of this section, but it should not affect the overall behaviour.

The conclusion drawn from our Fig. 11 and fig. 8 of Vega-Ferrero et al. (2019) is that the nature of mass clumpiness in the cluster can lead to $\sim$ 10–20 per cent variation in the predicted space number density of highly magnified sources at high redshifts.

5 EFFECT OF LENSING ON THE LUMINOSITY FUNCTION

Working as natural telescopes, clusters of galaxies can lens distant background galaxies magnifying their size and apparent brightness. Thus, otherwise unobserved galaxies come within the detection threshold of the contemporary telescopes, like the *HST*, by virtue of the magnification boost provided by the gravitational lenses.

The luminosity distribution for the background distant galaxies is described by the LFs. In this work, we are using the classical Schechter LF (Schechter 1976), which for a given redshift z_s can be

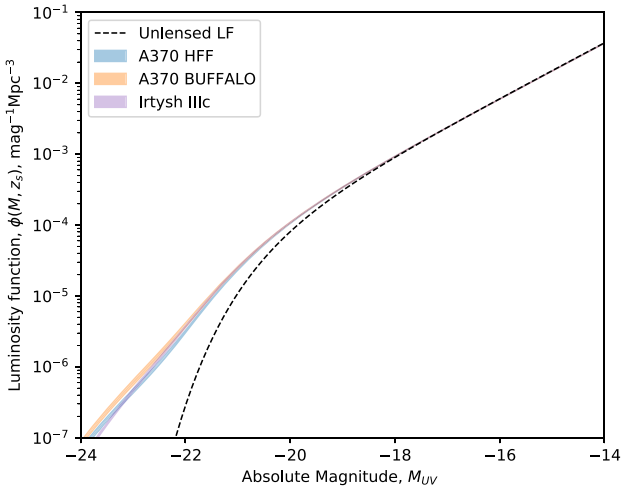

Figure 12. LFs at $z_s = 9.0$. Coloured shaded regions represent the uncertainties (68 per cent confidence range) in the lensed LFs for the GRALE reconstructions of A370 (HFF and BUFFALO models) and of Irtysh IIIc reconstruction. Black dashed line represents the classical unlensed Schechter function at a redshift of $z_s = 9.0$ and $\Delta z_s = 1.0$.

written in terms of absolute magnitude, M, as,

$$\phi(M, z_s) = 0.4 \ln(10) \phi^* 10^{-0.4(M-M_*)(\alpha+1)} e^{-10^{-0.4(M-M_*)}}, \quad (3)$$

where the values of normalization constant ϕ^*, characteristic magnitude M_*, and faint-end logarithmic slope α are the best-fitting parameters at the given redshift. In our work, their values are taken from Ishigaki et al. (2018). The use of the Schechter LF at high redshifts is further justified by Bouwens et al. (2015). The UV LF is shown as the black dashed line in Fig. 12, for redshift $z_s = 9.0$, with $\Delta z_s = 1.0$.

When distant galaxies with a given intrinsic LF get lensed by a cluster, their flux is magnified by a factor of μ and they gain an apparent magnitude of $-2.5\log_{10}\mu$. On the other hand, due to lensing the effective sampling volume reduces by a factor of $1/\mu$ (Broadhurst, Taylor & Peacock 1995). One can compute the lensed LFs $\phi'(M, z_s)$ by convolving the known unlensed LFs $\phi(M, z_s)$ with the distribution of the source plane magnifications at a given redshift of z_s and a given redshift interval of Δz_s,

$$\phi'(M, z_s) = \int_{\mu_{\min}}^{\mu_{\max}} \phi(M + 2.5 \log_{10} \mu, z_s) \frac{1}{\mu} \frac{d\sigma_{sp}(\mu, z_s)}{d\mu} d\mu, \quad (4)$$

where $d\sigma_{sp}(\mu, z_s)/d\mu$ is the area in the source plane with magnifications between μ and $\mu + d\mu$. Following the approach taken by Vega-Ferrero et al. (2019), the integral is computed in a range of $\mu_{\min} = 1$ to $\mu_{\max} = 100$. Demagnification is neglected since the field of view is limited to the regions where $\mu > 1$. While doing the integral in equation (4), we did not assume any magnitude cut off at either end of $\phi(M)$.

The shaded bands in Fig. 12 show the lensed LFs with uncertainties for the range of 40 reconstructions of A370 (HFFv4 and BUFFALO) and Irtysh IIIc. For example, at $M = -22.5$ the fractional uncertainty in lensed LFs is 0.078 for our A370 reconstruction with BUFFALO data; whereas it is 0.052 for the HFF reconstruction of A370 and 0.037 for Irtysh IIIc. All these values are at 68 per cent confidence range. The lensing affects the number density of the observed galaxies at a given absolute magnitude value. Some of the otherwise unobserved distant faint galaxies are pushed above the detection threshold due to the magnification and the already observed galaxies experience a flux increase and thus shifted towards a lower absolute magnitude. The change in the number of detectable galaxies depends on the faint-end logarithmic slope, α. A value of $\alpha = -2$ implies a magnification-independent LF (Broadhurst et al. 1995). In this work, we are using, $\alpha = -1.98$, as estimated by Ishigaki et al. (2018) for $z_s = 9.0$. Since in our case $\alpha > -2$, there will be a slight deficit of galaxies at fainter magnitudes. On the other hand at brighter magnitudes there is an excess of galaxies due to lensing. These explain why we see a deviation of the lensed LF from the unlensed LF in Fig. 12. These results are consistent with other works, for example, see section 4 of Vega-Ferrero et al. (2019).

6 CONCLUSIONS

Using the strong lensing image catalogues from the BUFFALO collaboration, we have performed the reconstruction of the galaxy cluster Abell 370 ($z_l = 0.375$) with our free-form algorithm GRALE. The LPrms is 0.45 arcsec, significantly lower than our HFF v4 reconstruction of the same cluster, which was 0.88 arcsec. Since the number of lensed images is nearly the same in both inversions, the improved LPrms is an indication of the improvement in the data quality of BUFFALO.

The reconstruction confirms the previously established active merging state of the cluster, as indicated by two large mass peaks separated by ∼200 kpc along the N-S direction. The fact that in our reconstructions the northern mass peak is displaced from the observed light peak of the northern BCG, could be a further indication of the disturbed state of the cluster. Though details vary, this displacement is also present in almost all the publicly available reconstructions of A370 (see Table 2), using parametric, free-form, and hybrid methods. Because this feature appears to be robust, it could provide another argument in favour of particle nature of dark matter, which uses baryonic matter as the source and cannot easily explain offsets between mass and light.

Our mass map shows two other interesting features. One, is a roughly critical density mass clump, of $M \sim 3 \times 10^{12}$ M$_\odot$, spanning ∼100 kpc, in the eastern side of the cluster (see Section 3.2). It was recovered independently in HFF reconstructions by free-form GRALE, hybrid WSLAP+, and is present in some parametric models as a cluster-scale dark matter halo. Our reconstruction using BUFFALO data also recovered this mass clump, further supporting its possibility.

The other mass feature is a probable filament (or similar external mass) stretching N-S through the cluster, and extending well outside the strong lensing region (see Section 3.3). Some of the publicly available reconstructions of A370 by other groups include similar features: external shear, or highly elongated mass 'fingers' going N-S through the cluster centre. Since our modelling window extends only somewhat beyond the strong lensing region, to account for the external mass GRALE generates mass clumps along the same direction, towards the lesser-constrained (containing few or no images) edges of the reconstruction window. To verify this hypothesis, we created the synthetic cluster, Irtysh III (see Section 3.4), with two external mass clumps, mimicking a filament. The recovered mass maps of Irtysh III are consistent with our expectations: GRALE produced mass clumps near the north and south edges of the modeling region, very similar to those in A370. (For Irtysh I, the synthetic cluster used in G20, where no external masses were included, GRALE did not produce this kind of extra N-S mass structures.)

Since the external mass responsible for the N-S mass clumps is well outside the multiple image region, its exact nature is not well constrained. It could be another galaxy cluster to the north or south of A370, or a large scale structure filament, with mass distributed

roughly evenly between north and south. Our reconstructions favour the latter, because individual GRALE runs place varying amounts of mass at the northern versus southern edges: there is no strong preference for one over the other. The galaxy distribution identified by Lagattuta et al. (2019) from the CFHT data, and extending NNW and SSE of the strong lensing region to the virial radius of the cluster, may be part of this potential filament structure.

While it is difficult to identify filaments in either ground-based or space-based optical or weak lensing data, our analysis suggests that it might be possible that the strong lensing data, used as part of parametric or free-form methods, has the potential to help identify filaments.

In Section 4.3 and 4.4, we consider the magnification properties of A370, as reconstructed by GRALE, and also relate the specific features of the magnification probability distribution, and magnification's dependence on source redshift on the properties of the mass distribution. In Section 4.3, using a very accurate forward lensing method, we calculate the source plane magnification distributions of Abell 370, and estimate the probabilities of magnifications, $\sigma_{sp}(\mu, z_s)$, i.e. the fraction of source plane area above a certain magnification value, at $z_s = 9.0$. We found that all the reconstructions exhibit the expected $\sigma_{sp}(\mu, z_s = 9.0) \propto \mu^{-2}$ behaviour at large magnifications ($\mu > 10$). At lower magnifications, the behaviour of σ_{sp} depends on the specifics of the recovered mass distribution. It differs slightly between the reconstructions, depending on whether the diamond caustics are enclosed by, or protrude outside of the oval caustic. We also explored the redshift dependence of $\sigma_{sp}(\mu, z_s)$ for a given magnification value of $\mu = 30$ (Section 4.4). When compared to other models, our magnification probabilities $\sigma_{sp}(\mu, z_s)$ tend to grow slower with redshift, implying that the substructure in GRALE reconstructions spans a wider range of scales compared to that of other reconstructions.

Finally, in Section 5, we estimated the uncertainties in the lensed LFs for our A370 reconstruction at a redshift of $z_s = 9.0$. We found the effect of lensing on the LFs with our reconstruction method to be in agreement with concurrent works by other groups.

One of the main conclusions from this work is based on the three mass features discussed above. We find it interesting, but do not fully understand why many reconstructions with distinct modelling philosophies – parametric versus free-form – can lead to converging results regarding specific mass features, for example the ∼100 kpc mass east of cluster centre, while at the same time, models of the same type using the same algorithm can draw contrasting conclusions, just by using slightly varied model priors and data constraints. Despite of this, we suggest that mass features that are common across the majority of different reconstructions – like at least two of the features considered here – can be considered as potential indicators of real structures.

We further conclude that because free-form models enjoy the freedom from fixed parameter spaces of parametric models, it enables them to recover mass features that are elusive for some parametric models, especially if the quantity and quality of lensing constraints is sub-optimal. All three mass features discussed in Section 3 were present in free-form reconstructions since the very first model by Abdelsalam et al. (1998), two decades ago, and all GRALE reconstructions, since HFFv1. But this freedom of free-form methods comes at a cost of lower spatial resolutions and possible overestimation of uncertainties. Free-form methods are also susceptible to producing artefacts when image number density is low. With upcoming observational facilities like the *James Webb Space Telescope*, which is expected to uncover hundreds of new strongly lensed images, free-form methods will be well positioned to accurately map out cluster mass distribution on scales greater than most individual galaxies.

ACKNOWLEDGEMENTS

The authors would like to thank the anonymous reviewer for their helpful comments that improved the paper. AG and LLRW acknowledge the support and the computational resources of Minnesota Supercomputing Institute (MSI) which were crucial for this work. MJ is supported by the United Kingdom Research and Innovation (UKRI) Future Leaders Fellowship 'Using Cosmic Beasts to uncover the Nature of Dark Matter' (grant number MR/S017216/1). GM received funding from the European Union's Horizon 2020 research and innovation programme under the Marie Skłodowska-Curie grant agreement No MARACAS - DLV-896778.

DATA AVAILABILITY

The lens inversion data underlying this article will be shared on reasonable request to the corresponding author. The strong lensing image set used in this work (see Table 1) is available as online supplementary material to this article.

REFERENCES

Abdelsalam H. M., Saha P., Williams L. L. R., 1998, MNRAS, 294, 734
Atek H., Richard J., Kneib J.-P., Schaerer D., 2018, MNRAS, 479, 5184
Bahcall N. A., Cen R., 1993, ApJ, 407, L49
Bartelmann M., 2010, Class. Quantum Gravity, 27, 233001
Bouwens R. J. et al., 2015, ApJ, 803, 34
Bouwens R. J., Illingworth G. D., Oesch P. A., Atek H., Lam D., Stefanon M., 2017a, ApJ, 843, 41
Bouwens R. J., Oesch P. A., Illingworth G. D., Ellis R. S., Stefanon M., 2017b, ApJ, 843, 129
Broadhurst T. J., Taylor A. N., Peacock J. A., 1995, ApJ, 438, 49
Diego J. M., 2019, A&A, 625, A84
Diego J. M. et al., 2018, MNRAS, 473, 4279
Faber S. M., Jackson R. E., 1976, ApJ, 204, 668
Fort B., Mellier Y., Picat J. P., Rio Y., Lelievre G., 1986, in Crawford D. L., ed., Proc. SPIE Conf. Ser. Vol. 627, Instrumentation in Astronomy VI. SPIE, Bellingham, p. 321
Ghosh A., Williams L. L. R., Liesenborgs J., 2020, MNRAS, 494, 3998 (G20)
Hammer F., 1987, in Bergeron J., Kunth D., Rocca-Volmerange B., Tran Thanh Van J., eds, Proc. IAP Workshop, High Redshift and Primeval Galaxies. Editions Frontieres, Gif-sur-Yvette, France, p. 467
Hammer F., Rigaut F., 1989, A&A, 226, 45
Hoekstra H., 2007, MNRAS, 379, 317
Ishigaki M., Kawamata R., Ouchi M., Oguri M., Shimasaku K., Ono Y., 2018, ApJ, 854, 73
Jauzac M. et al., 2015, MNRAS, 452, 1437
Johnson T. L., Sharon K., Bayliss M. B., Gladders M. D., Coe D., Ebeling H., 2014, ApJ, 797, 48
Kassiola A., Kovner I., 1993, ApJ, 417, 450
Kawamata R., Ishigaki M., Shimasaku K., Oguri M., Ouchi M., Tanigawa S., 2018, ApJ, 855, 4
Keeton C. R., 2001, preprint (arXiv:astro–ph/0102341)
Kneib J.-P., Natarajan P., 2011, A&AR, 19, 47
Kneib J. P., Mellier Y., Fort B., Mathez G., 1993, A&A, 273, 367
Kovner I., 1989, ApJ, 337, 621
Lagattuta D. J. et al., 2017, MNRAS, 469, 3946
Lagattuta D. J. et al., 2019, MNRAS, 485, 3738
Liesenborgs J., De Rijcke S., 2012, MNRAS, 425, 1772
Liesenborgs J., De Rijcke S., Dejonghe H., 2006, MNRAS, 367, 1209
Liesenborgs J., de Rijcke S., Dejonghe H., Bekaert P., 2007, MNRAS, 380, 1729

Liesenborgs J., Williams L. L. R., Wagner J., De Rijcke S., 2020, MNRAS, 494, 3253
Limousin M. et al., 2016, A&A, 588, A99
Livermore R. C., Finkelstein S. L., Lotz J. M., 2017, ApJ, 835, 113
Lotz J. M. et al., 2017, ApJ, 837, 97
Lynds R., Petrosian V., 1989, ApJ, 336, 1
Mahler G. et al., 2018, MNRAS, 473, 663
Medezinski E., Broadhurst T., Umetsu K., Benítez N., Taylor A., 2011, MNRAS, 414, 1840
Mellier Y., Soucail G., Fort B., Mathez G., 1988, A&A, 199, 13
Meneghetti M. et al., 2017, MNRAS, 472, 3177
Mohammed I., Liesenborgs J., Saha P., Williams L. L. R., 2014, MNRAS, 439, 2651
Mohammed I., Saha P., Williams L. L. R., Liesenborgs J., Sebesta K., 2016, MNRAS, 459, 1698
Natarajan P., Kneib J.-P., 1997, MNRAS, 287, 833
Navarro J. F., Frenk C. S., White S. D. M., 1996, ApJ, 462, 563
Press W. H., Schechter P., 1974, ApJ, 187, 425
Priewe J., Williams L. L. R., Liesenborgs J., Coe D., Rodney S. A., 2017, MNRAS, 465, 1030
Raney C. A., Keeton C. R., Brennan S., 2020a, MNRAS, 492, 503
Raney C. A., Keeton C. R., Brennan S., Fan H., 2020b, MNRAS, 494, 4771
Remolina González J. D., Sharon K., Mahler G., 2018, ApJ, 863, 60
Richard J., Kneib J. P., Limousin M., Edge A., Jullo E., 2010, MNRAS, 402, L44
Richard J. et al., 2014, MNRAS, 444, 268
Richard J. et al., 2021, A&A, 646, A83
Saha P., 2000, AJ, 120, 1654
Schechter P., 1976, ApJ, 203, 297
Schneider P., Ehlers J., Falco E. E., 1992, Gravitational Lenses. Springer-Verlag, Berlin
Sebesta K., Williams L. L. R., Mohammed I., Saha P., Liesenborgs J., 2016, MNRAS, 461, 2126
Sebesta K., Williams L. L. R., Liesenborgs J., Medezinski E., Okabe N., 2019, MNRAS, 488, 3251
Soucail G., 1987, The Messenger, 48, 43
Soucail G., Mellier Y., Fort B., Mathez G., Cailloux M., 1988, A&A, 191, L19
Steinhardt C. L. et al., 2020, ApJS, 247, 64
Strait V. et al., 2018, ApJ, 868, 129
Umetsu K., Broadhurst T., Zitrin A., Medezinski E., Hsu L.-Y., 2011, ApJ, 729, 127
Vega-Ferrero J., Diego J. M., Bernstein G. M., 2019, MNRAS, 486, 5414
Williams L. L. R., Liesenborgs J., 2019, MNRAS, 482, 5666
Williams L. L. R., Sebesta K., Liesenborgs J., 2018, MNRAS, 480, 3140
Wong K. C., Ammons S. M., Keeton C. R., Zabludoff A. I., 2012, ApJ, 752, 104
Zitrin A., Broadhurst T., 2016, ApJ, 833, 25
Zitrin A. et al., 2009, MNRAS, 396, 1985
Zitrin A. et al., 2013, ApJ, 762, L30

SUPPORTING INFORMATION

Supplementary data are available at *MNRAS* online.

BUFFALO_A370_SLimages.txt

Please note: Oxford University Press is not responsible for the content or functionality of any supporting materials supplied by the authors. Any queries (other than missing material) should be directed to the corresponding author for the article.

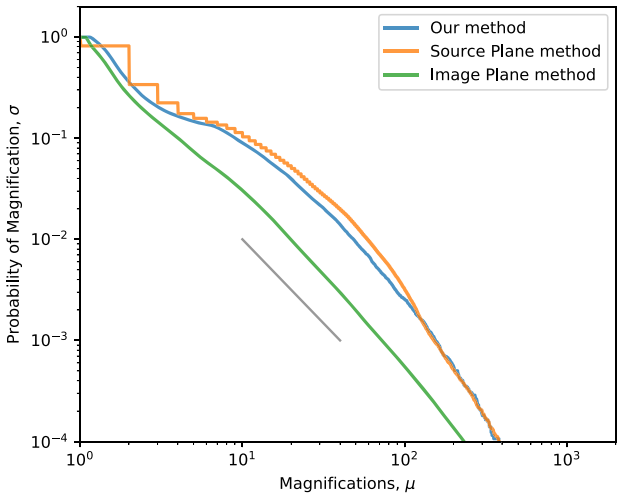

Figure A1. Comparison of the cumulative probability of magnifications in the source plane (similar to Fig. 10), as computed by our method and, the source plane method and the image plane method of Vega-Ferrero et al. (2019), using the average GRALE reconstruction of A370. The blue curves are the same as in Fig. 10. The grey line denotes a slope of μ^{-2}.

APPENDIX A: METHODS TO COMPUTE THE MAGNIFICATION DISTRIBUTION IN THE SOURCE PLANE

Here, we discuss a comparison between our method to compute the magnification distribution in the source plane and, the source plane method and the image plane method described in Vega-Ferrero et al. (2019).

In Vega-Ferrero et al. (2019), the authors use the magnification distribution in the image plane to retrieve the magnification distribution in the source plane. This is done either by back-projecting the image plane pixels to the source plane (source plane method), or by computing the area of a source plane by diving the corresponding area of the image plane pixels by the magnification value μ associated with it (image plane method). Image plane method is computationally cheaper of the two, and is widely used to compute magnification distribution in the source plane, for example, in the works of Johnson et al. (2014), Richard et al. (2014), Jauzac et al. (2015), etc.

In contrast to both of these methods, we compute the magnification by forward lensing the source plane grid points using the reconstructed deflection angles (see Section 4.1 for more details). Fig. A1 shows a comparison of the results for cumulative probability of magnifications in the source plane as computed by our method, the source plane method and the image plane method, using the average GRALE reconstruction of A370. As expected for a given mass distribution, our method and the source plane method produced very close results.

This paper has been typeset from a TEX/LATEX file prepared by the author.